

Indoor near-field target detection characteristics under radio and radar joint operation at 2.4 GHz ISM band

Dae Young Koh¹, Timothy S. Han², Joseph Zubah³

¹ Conestoga High School, Berwyn, Pennsylvania

² Electrical Engineering Department, Columbia University, New York, New York

³ Integrated Warfare Systems and Sensors Engineering, Rotary and Mission Systems, Lockheed Martin, Moorestown, New Jersey

SUMMARY

This paper presents an experimental research work on detecting an indoor near-field target at 2.4-GHz industrial, scientific, and medical (ISM) band. The research is based on hypotheses that if the detection target is in proximity to antennae, then the dominant electromagnetic (EM) wave couplings would happen between the target and antennas. Any other EM wave interaction between the antennas and indoor background objects would be secondary to the target-to-antennas EM-wave interaction. This unique coupling may allow us to distinguish and measure the EM wave energy scattered by the target to the receive antenna in the form of signal power using a spectrum analyzer. The detection power is a strong function of the distance between the target and receiving antenna, which could be characterized by radar equations. In such scenario, the hardware module configured to test the hypotheses plays the role of a radar sensor that detects indoor targets at near-field region under the coexistence and cooperation of WiFi radio link at the ISM band. In the experiment, at the presence of a flat round metal target with radius 5 cm, the measured detection signal power ranged from 10 nW to 1 mW (-30 dBm) when the sensing distance (r) decreased from the edge of a radiative near-field ($r = \lambda = 12.5$ cm) to the reactive near-field region ($r = \lambda/2\pi = 2$ cm). These were well-agreeable with theoretical estimations by radar equations, validating the hypotheses.

INTRODUCTION

This paper presents an experimental study on detecting indoor targets electromagnetically. In this experiment, we are particularly interested in the empirical modeling of EM wave interactions between the antenna and target at 2.4 GHz industrial, scientific, and medical (ISM) band. The engineering motivation of utilizing 2.4-GHz ISM band signals is that upon successful experiment, it qualifies a new radar sensing modality suitable for cost-effective target detection at near-field while supporting the radar and radio coexistence and cooperation. The target detection experiment is based on the following hypotheses. First, if a detection target is close enough to the transmitting (Tx) and receiving (Rx) antennas, then the electromagnetic (EM) wave interaction

between the antennas and the target will dominate over the EM wave interactions amongst the Tx-Rx antennas and other background indoor objects. Second, then, we may be able to discriminate the received EM wave energy by the target from background noises, which could be characterized using radar equations (1).

Traditionally, radios and radars have been regarded as two independent wireless entities and operated at mutually exclusive frequency bands because radio and radar signals can interfere with each other in a destructive manner—degrading receive signal quality of the other system significantly. However, increasing demands on the wireless communication data rates have motivated some to harness the radar spectrum resources and sputtered research on the cooperation or coexistence of those two previously incompatible wireless systems by sharing the same frequency bands (2).

Substantial research efforts have been made to resolve the radio and radar mutual interference issues with advanced signal processing techniques over various coexistence system platforms, including cognitive radios, electrically-steerable analog beamformers, or dual-function radar communication (DFRC) systems (3-5). The DFRC systems combine the radar and radio transmitters in the same hardware, resulting in a compact and cost-effective system solution that is possibly suitable for a mobile terminal (6). In general, the signal bandwidth of a radar will be much wider than that of a radio to achieve a high radial or angular detection resolution. Typical radar-radio dual systems leverage adaptive beamforming with sidelobe control or waveform diversity to embed communication data within radar pulse trains, requiring rather complex digital signal processors (DSPs) (7). The radar-radio joint system configuration, however, can be much simpler when the radar function is limited to localizing an indoor target with a single-tone continuous-wave (CW) radar module wherein the narrowband monotone radar signal can be easily separated from the modulated communication signals by orthogonal code diversities (8).

The single-tone CW radars have been popular for medical tomographic imaging or physiologic sign detection through Doppler frequency shifts (9,10). However, there has been a lack of research effort on utilizing the single-tone CW radars for a dual usage of radar and radio joint operation. Recently, the demand for the wireless communication and sensing joint functionality is increasing because contemporary fifth-generation wireless devices would require the joint functionality to enable various human-machine, machine-

machine, or machine-sensor communications with situational awareness (11).

Driven by these needs, our hypothesis is being tested by the hardware assumed to be built in the DFRC system framework using 2.4-GHz ISM band signals for dual purpose of radar sensing while maintaining seamless WiFi radio links at the same band. Validation of the hypothesis with 2.4-GHz CW sinusoidal tone will qualify the radar-radio joint operation with no extra spectrum cost and minimizing additional spectrum emission at the ISM band. As detailed in the following sections, to detect a large-scale motion or target, the radar sensor module that is configured to validate the hypothesis is initially calibrated to an EM wave balance state. Presence of a target at the near-field of the radar will break the EM wave balance state. The present radar operation is unique because it recognizes a target by measuring the degree of EM wave disturbance caused by the target, while conventional radars measure either time or phase delay of the signal reflected by the target. The aiming applications include noncontact, automatic wakeup systems like computer, laptop, or mobile terminal monitor wakeup sensors; gesture or security motion sensors; or Internet of Thing (IoT) sensor activation stimulators.

RESULTS

The experiment was conducted in indoor laboratory environment with turning on a 2.4-GHz IEEE 802.11b/g/n wireless router to measure the target detection characteristics under a sensing and communication joint environment. The router was located in the same experiment room and the line-of-sight distance between the router and antennas was approximately 2 m without obstacles between. The detection target is a flat circular metal object (radius: 5 cm) which is approached from a line-of-sight distance r to the antennae (Figure 1). The wavelength (λ) of radar signal at 2.4 GHz is $\lambda = c/f = 12.5$ cm, where c is the light speed (3×10^8 m/s) and f is the radar signal's linear frequency of 2.4 GHz. The near-field and far-field regions are distinguishable by the relative distance of the target position r compared with λ . Namely,

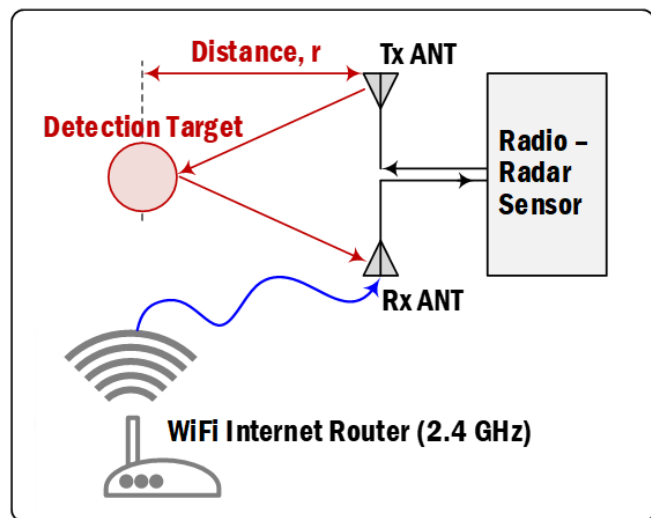


Figure 1. Conceptual experiment setup for indoor target detection.

when $r \leq \lambda$ the target is considered at a near-field region, while when $r > \lambda$ the target is considered at a far field area (12). Two examples of the measured output spectrum for the near-field ($r = 3$ cm) and far-field ($r = 30$ cm) cases are shown and the radar detection signal is noted as \textcircled{a} and WiFi signals are noted as \textcircled{b} (Figure 2). In the experimented radar-radio coexistence environment, the detection threshold power was increased by the ambient WiFi radio signal power level. The measured environment WiFi signal power at 2.4000–2.4835 GHz is around 1 nW (-60 dBm) and the detection powers (P_d) at the near- and far-fields are about 1 mW (-30 dBm) and 10 nW (-50 dBm), respectively (Figure 2A,2B).

More comprehensive detection characteristics measured by varying r is shown in Figure 3. A typical radar equation for the output power detected by sensing targets at a far field region can be given as

$$P_d = P_t G_t \sigma A_{\text{eff}} / (4\pi r^2)^2 = K / r^4 \quad (\text{Eq-1})$$

where P_t is a transmit signal power by a radar transmitter; G_t is a transmitting antenna gain; σ is a radar cross sectional area of a target; and A_{eff} is an effective receiving antenna area (1). σ is dependent on material properties of a target and can vary over sensing distance, making it difficult to model at a near field area (13). Furthermore, the sensor module

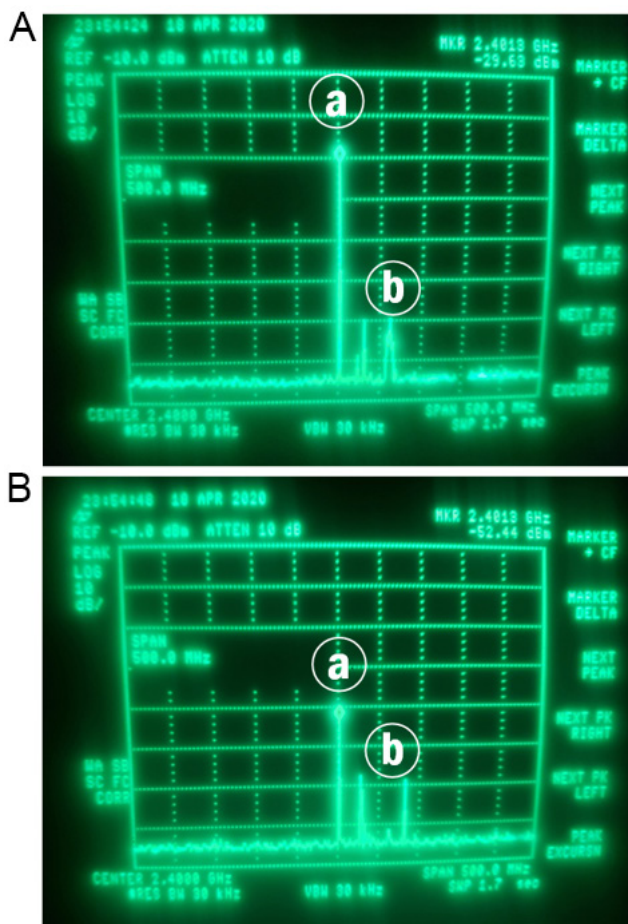


Figure 2. Exemplary measured target detection output spectrum with cooperating 2.4 GHz WiFi signal reception: (A) when target is at near field area ($r \leq 12.5$ cm) and (B) when target is at transition zone or far field area ($r > 12.5$ cm).

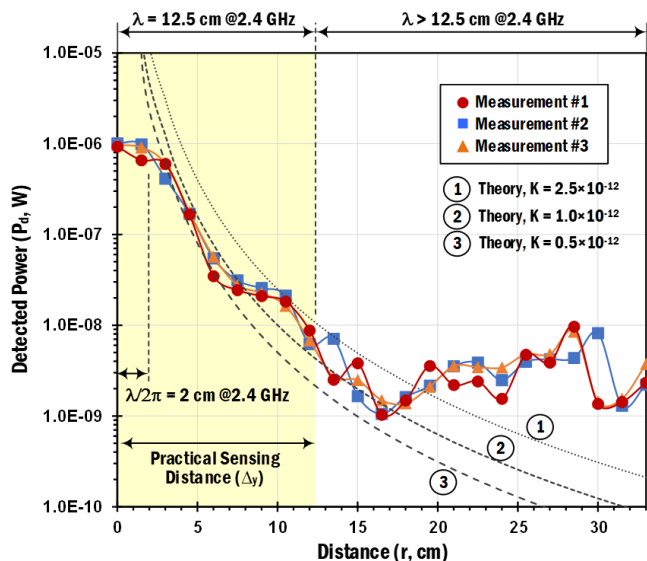


Figure 3. The measured target detection characteristics at 2.4 GHz. Three different measurements are numbered as #1, #2, and #3, respectively.

detects proximity targets at the indoor environment where electromagnetic wave propagation is quite complicated and heavily dependent on the surrounding objects. Under environmental uncertainty, an exact modelling of the radar equation parameters in the near field areas is challenging and beyond the scope of this work. Thus, the material parameter σ and the other antenna and transmit parameters are lumped to a curve-fitting parameter K determined empirically through experiments in the above equation. The theoretical detection power with several different K , calculated using Eq-1, is also plotted together for comparison purpose (Figure 3). From the measured data, it is observed that when $r \leq 2$ cm, P_d saturates to 1 mW and therefore it is not possible to decrease detection range resolution < 2 cm. Nevertheless, P_d is well-estimated by Eq-1 in the region of $2 \text{ cm} \leq r \leq 15 \text{ cm}$ with $0.5 \times 10^{-12} \leq K \leq 2.5 \times 10^{-12}$.

DISCUSSION

The intended near-field detection range ($r \leq 12.5$ cm) is highlighted in yellow color (Figure 3). In principle, we can divide the near field region into three different sectors: reactive near-field, radiative near-field, and transition zones, depending on distance to the antennas. From the measured results, the following observation can be made in each region.

When the target is in a reactive near-field region, $r \leq \lambda/2\pi = 2$ cm, the dominant EM wave radiation mode is a reactive signal coupling, a combination of capacitive and inductive signal coupling between Tx and Rx antennas and the target (Figure 3). In this case, the signal characteristics of the transmit and receive detection signals are similar to those of radar calibration mode (Figure 5A,5B). A good phase coherence between the received signal and control path signal can be maintained. Thus, a part of received target detection signal energy will be subtracted continuously by the energy of the calibration path signal, resulting in a saturated detection power of around $P_d = 1 \mu\text{W}$ (-30 dBm) in steady states.

When the target is within the range of radiative near-field

($\lambda/2\pi \leq r \leq \lambda$), the received radar signal experiences a phase delay during the journey from the Tx antenna to the target and from the target to the Rx antenna. This will disturb the phase coherence between the detected signal and control path signal and the detected radar signal powers are well-estimated by the quartic dependency over r in Eq-1. In this region, P_d ranges from 10 nW to 1 μW , well-agreeable with the radar equation with K varying from 0.5×10^{-12} to 2.5×10^{-12} [W/m^4] over the sensing distance r increases from $\lambda/2\pi$ to λ .

Finally, when the target is beyond near-field and located at transition zone or far-field region, P_d decreased to < 10 nW (-50 dBm) and fluctuated between 1–10 nW depending on the time-varying ambient WiFi radio signal power level. This inevitably forces us to set the minimum detectable signal power level to 10 nW, which is barely distinguishable from the ambient noises and defines a detection threshold of the proximity radar sensor.

The experiment supports the hypothesis that the EM wave sensor works properly by detecting a target in the near-field area $< r = 12.5$ cm with the detection power level > 10 nW, while desensitizing targets at a far-field region. Figure 4 cartoons one typical application example of the EM sensor and provides rationale for the proximity target sensing in a near-field region ranging approximately one wavelength of the 2.4 GHz ISM band signal. In typical ergonomic laptop setups, the distance between a laptop monitor and the user's face, Δ_x in Figure 4, is in the order of ≥ 50 cm. A distance of action (DoA) defined by the distance from a monitor to a user's hands for a reliable wakeup or noncontact control action, Δ_y in Figure 4, should be much shorter than Δ_x . In usual sensing operations, the sensors must desensitize any background motion provoked by surrounding objects in the range of Δ_x while detecting a motion or a target within the Δ_y DoA. The one wavelength distance at 2.4 GHz is be a reliable and comfortable DoA for users. At the same time, the unlicensed ISM band allows a shared dual usage of spectrum for the radar sensing and WiFi communication with no particular spectrum regulatory being required if the radar mode transmit power level is < 1 W (14).

Finally, the human body can be regarded as a conductor being composed of 70% water comprised of various charged ions like sodium, potassium, chloride, etcetera; however, it may not be as perfect a conductor as the metal object used in this experiment. We propose as further research work to experiment target detection characteristics by approaching

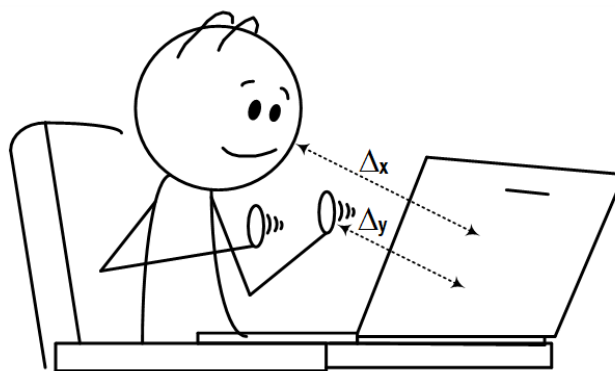


Figure 4. Application example of the proposed electromagnetic (EM) wave sensor: noncontact laptop monitor wakeup sensor being stimulated by handshaking at a near-field distance.

actual human hands to fully explore the feasibility of the system as a wake-up sensor.

MATERIALS AND METHODS

Hardware Configuration and Operations

The RF front-end building blocks for sensing targets in proximity are illustrated in **Figure 5**. For practical applications, the sensing system should be able to detect a target or a motion in the order of 1–100 cm range without disturbing wireless communication functions. To support the joint operation of radio communication and radar sensing, the building blocks are built upon a DFRC system platform wherein a series of DSPs inside DFRC transceiver provides an orthogonal code diversity between radar and radio signals so that they can be decorrelated and classified separately at the DFRC receiver end (4,5).

The first step for the RF system to operate as a radar sensor is to characterize its detection threshold. For this, the RF front-end system adopts a delay (τ) controller cascaded by an amplitude (α) controller (**Figure 5A**). In the radar calibration mode, the time slot of ② depicted in the control timing diagram in **Figure 5C**, a DFRC transceiver generates a pilot signal $f_{cal}(t)$ from node ③ to evaluate a transmit (Tx)-to-receive (Rx) leakage signal caused by the coupling between the Tx and Rx antennas. A Tx directional coupler couples a fraction of $f_{cal}(t)$ to the controller path which develops a calibration signal of $\alpha_{cal} \cdot f_{cal}(t - \tau_{cal}) \cdot \tau_{cal}$ at node ④ in **Figure 5A**. τ_{cal} and α_{cal} express the time delay and amplitude control parameters, respectively, set by each τ and α controller in **Figure 5A**. The Tx-to-Rx leakage signal at node ⑤ can be represented as $\alpha_{cpl} \cdot f_{cal}(t - \tau_{cpl}) \cdot \alpha_{cpl}$. α_{cpl} expresses a coupling magnitude and τ_{cpl} represents overall delay effect of the leakage signal from the antenna coupling node to the input of a 180°-hybrid coupler. The Cx directional coupler provides a reference signal of $\beta_{cal} \cdot f_{cal}(t - \tau_{cal})$ to node ⑥ so that the DFRC transceiver to estimate Tx-to-Rx leakage with referencing to the controller signal. Then, the DSP units inside DFRC receiver adjust α and τ parameters in a closed loop manner to match $\alpha_{cal} \cdot f_{cal}(t - \tau_{cal})$ with $\alpha_{cpl} \cdot f_{cal}(t - \tau_{cpl})$, e.g. $\alpha_{cal} = \alpha_{cpl}$ and $\tau_{cal} = \tau_{cpl}$ in ideal operation (15,16). One characteristic function of 180°-hybrid couplers is signal subtraction and the input signals at the nodes ④ and ⑥ in **Figure 5A** are finally subtracted and cancelled out at the delta (Δ) port (node ⑤) of the 180°-hybrid coupler. In practice, however, the rejection of Tx-to-Rx leakage signal is finite due to limited time and amplitude matching of those signals at the inputs of the 180°-hybrid coupler. This finite rejection essentially sets a target detection threshold ($P_{d,th}$) in the given system, expressed in decibel (dB) scale as:

$$P_{d,th} = 20 \cdot \log |\alpha_{cpl} \cdot f_{cal}(t - \tau_{cpl}) - \alpha_{cal} \cdot f_{cal}(t - \tau_{cal})| \text{ (dB)} \quad (\text{Eq-2})$$

Once determining the sensor detection threshold, the focus of this work is to experimentally characterize detection characteristics at the presence of a proximity target near the antennas, by varying the target distance r as illustrated in **Figure 5b**. After the calibration process settles down, α_{cal} and τ_{cal} are fixed. The sensor reaches an EM-wave equilibrium state where the electromagnetically coupled Tx-to-Rx leakage signals are balanced out by the internal controller output signals to the point of the detection threshold level. The presence of target disturbs the EM-wave equilibrium state. The transmit radar signal $f_{det}(t)$ will travel a certain distance to the target and be reflected to the receive antenna

by the target (**Figure 5b**). A reasonable hypothesis is that the amplitude (α_{det}) and delay (τ_{det}) factors of the detection signal will be statistically different from those of the calibration mode, resulting in a measurable output power P_d at the 180°-hybrid coupler output, which can be expressed as:

$$P_d = 20 \cdot \log |\alpha_{det} \cdot f_{det}(t - \tau_{det}) - \alpha_{cal} \cdot f_{cal}(t - \tau_{cal})| \text{ (dB)} \quad (\text{Eq-3})$$

α_{det} is a strong function of r , and P_d is governed by the radar equation of Eq-1, exhibiting a quartic dependency of r . However, when the target is very close to the antennas and $r \leq \lambda/2\pi$, the signal interaction between antennas and target is by reactive coupling, rather than EM wave radiation (12). In such case, τ_{det} can be close to τ_{cal} because of relatively short traveling distance, resulting in a good phase coherence between the control path signal and the target detection signal from Rx antenna. In general, the closer r is, the stronger P_d will be detected. However, because of better signal coherence, the detected signal will be subtracted more by the control signal, leading to a saturation of the detected power in the reactive near-field region (**Figure 3**).

Experimental Setup

The experimental setup is built on a Lego™ substrate and configured using commercially available off-the-shelf (COTS)

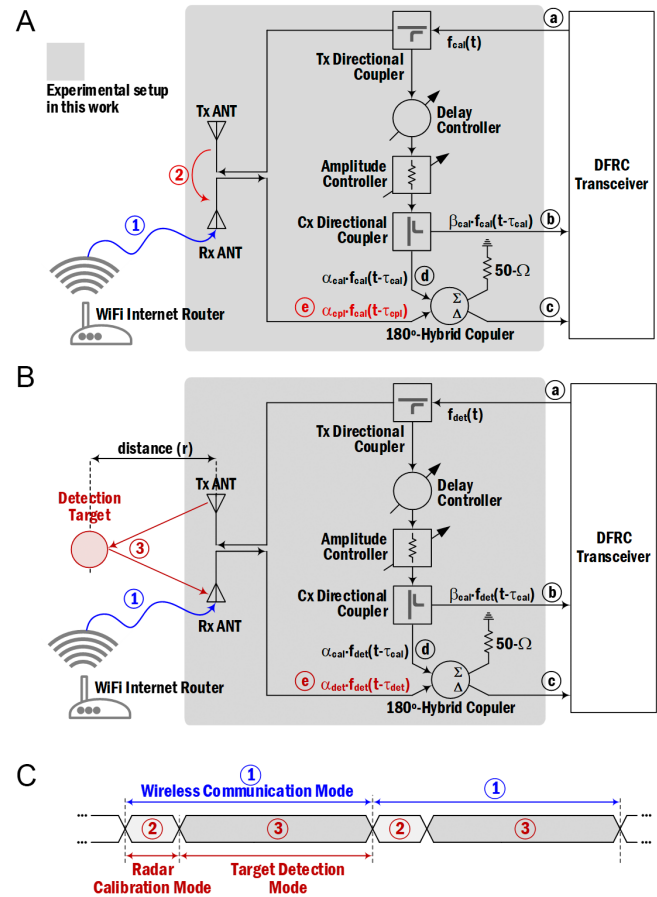


Figure 5. RF front-end building blocks for proximity target detection under the radio and radar joint operations. (A) radar calibration mode, **(B)** target detection mode, **(C)** time-shared radar mode timing diagram for joint operation of radar sensing and wireless communication.

RF components. The cascading of COTS RF components in the experimental setup shown in **Figure 6** is matched exactly with that of the group of RF front-end building blocks in gray area in **Figure 5**. For Tx and Rx antennas, TP-Link dual-band antennas (model: TP-Link Archer TX3000E) are used. The antennas support 2.4 GHz WiFi radio signal transmission and reception with 5 dBi of antenna gain. Antenna gain is a measure of the directivity of radiated signal power—the ratio of a radiated signal power by the WiFi antenna to a theoretical omnidirectional signal power by a hypothetical ideal radiator. A Mini-Circuits ZAPD-4 power splitter and a MERRIMAC directional power splitter are used for the Tx and Cx directional power couplers, respectively. For the intended narrowband radar sensing operation, a continuous analog phase shifter from KDI/Triangle Inc. adjusts time delay approximately by controlling phase shift at 2.4 GHz. For amplitude control, an RF-variable attenuator from JFW Industries Inc. is used (model: 50AP-077 SMA). A 180o-hybrid coupler from SIGA Tech. Inc., model: SH12552, combines signals from the Rx antenna and controller paths, eliminates a common mode component, and produces a difference signal measured using an HP 8593A spectrum analyzer. The effective isotropically radiated transmit power, P_{iG} in Eq-1, of the antennas is set to -10 dBm at 2.4 GHz in this experiment. In the radar calibration mode, the control voltages of the phase shifter and attenuator are calibrated so the output from the D-port of the 180°-hybrid coupler becomes < -50 dBm at the -10 dBm transmit power. This output results in 40 dB rejection of Tx-to-Rx leakage in the calibration mode. In the detection mode, a flat circular metal object (radius: 5 cm) is approached from a line-of-sight distance r to the antennas while measuring the output spectrum from the 180°-hybrid coupler using HP 8593A.

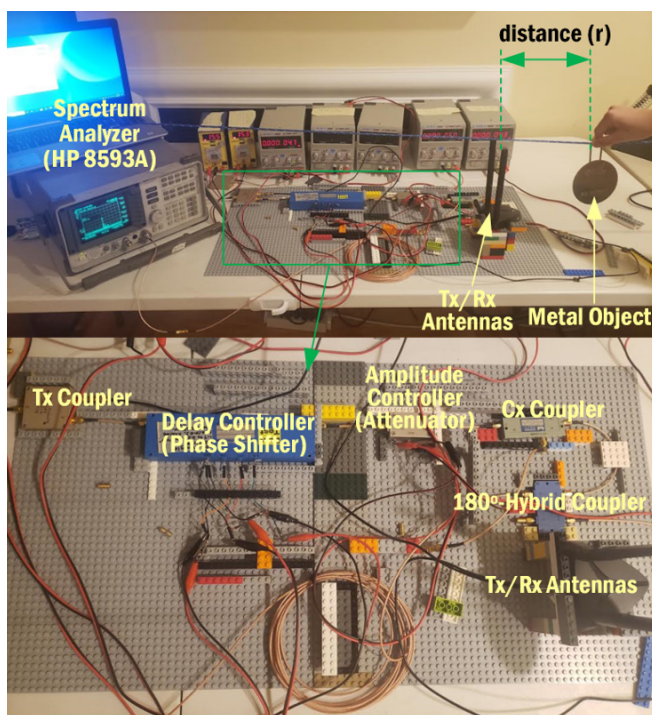


Figure 6. Experiment setup configured using COTS RF components.

ACKNOWLEDGMENTS

This work is supported technically by a voluntary Lockheed Martin's Science, Technology, Engineering and Mathematics (STEM) outreach program. I would like to thank my father and my mother for their technical advice and equipment support during this STEM project.

Received: May 22, 2021

Accepted: Sep 21, 2021

Published: April 29, 2022

REFERENCES

1. Richards, Michael A., *et al.*, editors. *Principle of Modern Radar: Basic Principles*, 1st ed. SciTech Publishing, Inc., 2010.
2. Chiriyath, Alex R., *et al.* "Radar-Communication Convergence: Coexistence, Cooperation, and Co-Design," *IEEE Transactions on Cognitive Communications and Networking*, vol. 3, no. 1, 2019, pp. 1-12, doi: 10.1109/TCCN.2017.2666266.
3. Yao, Yu, *et al.* "Cognitive Waveform Optimization for Phase-Modulation-Based Joint Radar-Communication System," *IEEE Access*, vol. 8, 2020, pp. 33276-33288, doi: 10.1109/ACCESS.2020.2974787.
4. Hassanien, Aboulnasr, *et al.* "Dual-Function Radar-Communications: Information Embedding Using Sidelobe Control and Waveform Diversity," *IEEE Transactions on Signal Processing*, vol. 64, no. 8, 2016, pp. 2168-2181, doi: 10.1109/TSP.2015.2505667.
5. Tian, Tuanwei, *et al.* "Power Distribution for an OFDM-Based Dual-Function Radar-Communication Sensor," *IEEE Sensors Letters*, vol. 4, no. 11, 2020, doi: 10.1109/LSENS.2020.3033044.
6. Nusenu, Shadrack Yaw, *et al.* "Dual-Function Radar-Communication System Design Via Sidelobe Manipulation Based On FDA Butler Matrix," *IEEE Antenna and Wireless Propagation Letters*, vol. 18, no. 3, 2019, pp. 452-456, doi: 10.1109/LAWP.2019.2894015.
7. Liu, Fan, *et al.* "On Range Sidelobe Reduction for Dual-Functional Radar-Communication Waveforms," *IEEE Wireless Communication Letters*, vol. 9, no. 9, 2020, pp. 1572-1576, doi: 10.1109/LWC.2020.2997959.
8. Mietzner, Jan, and Avik Santra. "Space-Time Waveform Coding for Joint Radar and Wireless Communications (RadCom) Applications," *2020 IEEE Wireless Communications and Networking Conference (WCNC)*, IEEE, 2020, doi: 10.1109/WCNC45663.2020.9120568.
9. Scudder, H. J. "Introduction to computer aided tomography," *Proceeding of the IEEE*, vol. 66, no. 6, 1978, pp. 628-637, doi: 10.1109/PROC.1978.10990.
10. Tu, Jianxuan, *et al.* "Respiration Rate Measurement Under 1-D Body Motion Using Single Continuous-Wave Doppler Radar Vital Sign Detection System," *IEEE Transactions on Microwave Theory and Technique*, vol. 64, no. 6, 2016, pp. 1937-1946, doi: 10.1109/TMTT.2016.2560159.
11. Thoma, Seiner S., *et al.* "Cooperative Passive Coherent Location: A Promising 5G Service to Support Road Safety," *IEEE Communications Magazine*, vol. 57, no. 9, 2019, pp. 86-92, doi: 10.1109/MCOM.001.1800242.
12. "Near and far field." *Wikipedia: The Free Encyclopedia*, Wikimedia Foundation, <https://en.wikipedia.org/wiki/>

Near_and_far_field (Accessed Feb. 10, 2020).

13. Deban, Ramin, *et al.* "Deterministic Approach for Spatial Diversity Analysis of Radar Systems Using Near-Field Radar Cross Section of a Metallic Plate," *IEEE Transactions on Antennas and Propagation*, vol. 58, no. 3, 2010, pp. 908-916, doi: 10.1109/TAP.2009.2039328.
14. Federal Communications Commission, Office of Engineering Technology Laboratory Division. "Guidance for IEEE 802.11ac™ and Pre-ac Device Emission Testing.", <https://apps.fcc.gov/eas/comments/GetPublishedDocument.html?id=253&tn=355914> (Accessed May 4, 2019).
15. Bharadia, Dinesh, *et al.* "Full Duplex Radios," *ACM SIGCOMM Computer Communication Review*, vol. 43, no. 4, 2013, pp. 908-916, doi: 10.1145/2534169.2486033.
16. Choi, Yang-Seok, and Hooman Shirani-Mehr. "Simultaneous Transmission and Reception: Algorithm, Design and System Level Performance," *IEEE Transactions on Wireless Communications*, vol. 12, no. 12, 2013, pp. 5992-6010, doi: 10.1109/TWC.2013.101713.121152.

Copyright: © 2022 Koh, Han, and Zubah. All JEI articles are distributed under the attribution non-commercial, no derivative license (<http://creativecommons.org/licenses/by-nc-nd/3.0/>). This means that anyone is free to share, copy and distribute an unaltered article for non-commercial purposes provided the original author and source is credited.